Dalton Transactions

ROYAL SOCIETY OF CHEMISTRY

FRONTIER

View Article Online
View Journal | View Issue

Cite this: *Dalton Trans.*, 2026, **55**, 5863

Reaction channels of iron-oxo and iron-imido molecular intermediates

Thomas D. Jones, Henry R. Brothers, Elokkin K. Pate-Geames, David M. Jenkins* and Konstantinos D. Vogiatzis *

Non-heme Fe(IV)-oxo intermediates are integral components of many enzymatic and homogeneous catalytic cycles, where they serve as key oxidants that enable challenging transformations. Numerous studies have focused on developing biomimetic non-heme Fe(IV)-oxo catalysts, elucidating their electronic structures, and understanding the nature of their reactivity. Their high-valent nature endows them with the capacity to perform demanding oxidative transformations, as evidenced by their broad application in C–H activation and alkene epoxidation chemistry. The isoelectronic Fe(IV)-imido analogue is much less studied, presenting significant opportunities for catalyst development in nitrene-transfer chemistry, including C–H amination and alkene aziridination. Mechanistically, nitrene transfer involves an Fe-imido intermediate featuring an N-centered radical. Two competing pathways have been described: a σ-channel and a π-channel, defined by whether the radical character is localized in a σ* or π* orbital. Similar to Fe(IV)-oxo chemistry, the reaction channel preference among Fe(IV)-imido catalysts plays a crucial role in determining their reactivities and selectivities. Herein, the nitrene transfer pathways for these species within both reaction channels are explored and comparative examples between Fe(IV)-oxo and Fe(IV)-imido catalysts are discussed.

Received 9th December 2025,
Accepted 10th March 2026

DOI: 10.1039/d5dt02942b

rsc.li/dalton

Introduction

Iron-oxo intermediates are key reactive species in numerous heme and non-heme enzymatic systems, valued for their potent oxidizing power and their capacity to functionalize a broad range of substrates.[1,2] Non-heme iron-oxo containing enzymes lack a porphyrin ligand and most commonly consist of two or three nitrogenous histidine residues and a carboxylate-containing residue, such as from aspartate or glutamate, in the primary coordination sphere.[3,4] The iron-oxo intermediates in non-heme enzymes are usually found in the +IV oxidation state and exhibit a high-spin state ($S = 2$).[5–8] The high-spin Fe(IV) active sites found in non-heme enzymes are highly reactive and are capable of catalyzing a large array of oxidation reactions, including C–H activation, alkene epoxidation, halogenation, ring formation, and ring expansion.[9–11]

Non-heme Fe-(IV)oxo species are commonly formed *via* O_2 activation, proceeding through Fe(III)-peroxo or Fe(III)-superoxo intermediates which are subsequently reduced by external cofactors (NADH, ascorbate) to hydroperoxo or organoperoxo intermediates before generating the Fe(IV)-oxo complex.[2,9] For C–H activation of alkane substrates, the Fe(IV)-oxo site typically abstracts a hydrogen from an alkane for the formation of a Fe(III)-hydroxo intermediate followed by a rebound step in C–H hydroxylation or by formation of a carbon–halogen bond in C–H halogenation reactions. In epoxidation reactions, the Fe(IV)-oxo activates the double bond of an alkene to create a radical organoperoxo followed by a ring closing step. The rate determining step is typically hydrogen abstraction or alkene activation.[12–14] Extending beyond oxygen transfer, iron-imido intermediates provide nitrene-based analogues that are isoelectronic to iron-oxo species. Iron-imido species are less commonly encountered than their iron-oxo counterparts; nonetheless, iron-imido intermediates have been proposed in certain nitrogen-fixation pathways mediated by nitrogenase enzymes.[15] Given the extensive mechanistic foundation established for Fe(IV)-oxo intermediates, their σ/π-channel reactivity provides a benchmark for evaluating and comparing Fe(IV)-imido reactivities herein. Because of their central role in numerous enzymatic transformations, non-heme iron-oxo species have been investigated in great depth.[4,9] However, spectroscopic analysis and characterization of the intact metalloenzyme is often challenging. The even spin ($S = 2$) associated with these enzymes render traditional EPR impossible, while ligand–metal charge transfer (LMCT) in the UV-vis spectra for these systems is often inaccessible.[16] Therefore, smaller biomimetic transition metal model complexes have been developed to help understand enzyme active site composition and the related reaction mechanism by mimicking the structural features of the first and second coordination spheres. Additionally, if the

Department of Chemistry, University of Tennessee, Knoxville, Tennessee 37996-1600, USA. E-mail: djenki15@utk.edu, kvogiatz@utk.edu

nature of the active site is not known, smaller model complexes can help understand the nature of the active site by comparing experimental or theoretical spectra from the model system to the enzyme's spectrum. Beyond structural mimicry, these models aid in elucidating reaction mechanisms and offer a controlled platform to efficiently isolate, characterize, and rationalize key intermediates. More importantly, understanding the structures and reactivities of these enzymes enables the rational design and synthesis of bioinspired catalysts capable of emulating enzymatic function.

Due to iron's terrestrial abundance, non-toxicity, and the high reactivities of iron-oxo containing enzymes, synthetic chemists have developed numerous bioinspired non-heme iron-oxo catalysts which mimic the catalytic activities of targeted enzymes. Bioinspired catalysts can exceed metalloenzymes because they enable substrate scope expansion beyond enzymatic feasibility and can exhibit unique chemo- or regioselectivities for preparation of new and more diverse products. While synthetic Fe(IV)-oxo intermediates in the triplet spin state were the first to be isolated, numerous high spin quintet Fe(IV)-oxo complexes, as well as Fe(V)-oxo and a few Fe(III)-oxo complexes, have since been developed. These complexes typically consist of neutral (for Fe(IV)) or anionic nitrogenous ligands (more typical for Fe(V) or Fe(III) cases) in a *pseudo*-octahedral or *pseudo*-trigonal bipyramidal geometry (Fig. 1). These synthetic analogues have been used extensively in catalyzing two electron oxidation processes such as C–H bond activation,[17–20] epoxidation,[21–24] and halogenation reactions.[25–29] Synthetically, these catalysts are often formed using strong oxidizing agents like peroxides or hypervalent iodine compounds. Due to their similarities to nitrogenase enzymes, iron-imido complexes (Fig. 1) have found utility in the syntheses of high-value nitrogen containing molecules. Among these, iron-imido complexes have been suggested as potential intermediates in the Haber–Bosch process[30] and homogenous nitrogen fixation reactions.[31–34] Furthermore, based on the successes of non-heme iron-oxo intermediates for alkane hydroxylation and alkene epoxidation reactions, analogous non-heme iron-imido systems have been developed. Synthetic iron-imido complexes routinely bear anionic ligands or strong σ-donors like phosphines and N-heterocyclic carbenes to stabilize the iron-imido. Moreso than iron-oxo complexes, iron-imido complexes cover a wide variety of geometries and oxidation and spin states (Fig. 1). Furthermore, iron-imido complexes have been demonstrated as competent catalysts for nitrene transfer reactions such as C–H amination[35–37] and alkene aziridination.[38–42]

Building on these experimentally characterized intermediates, computational methods provide deeper insight into their

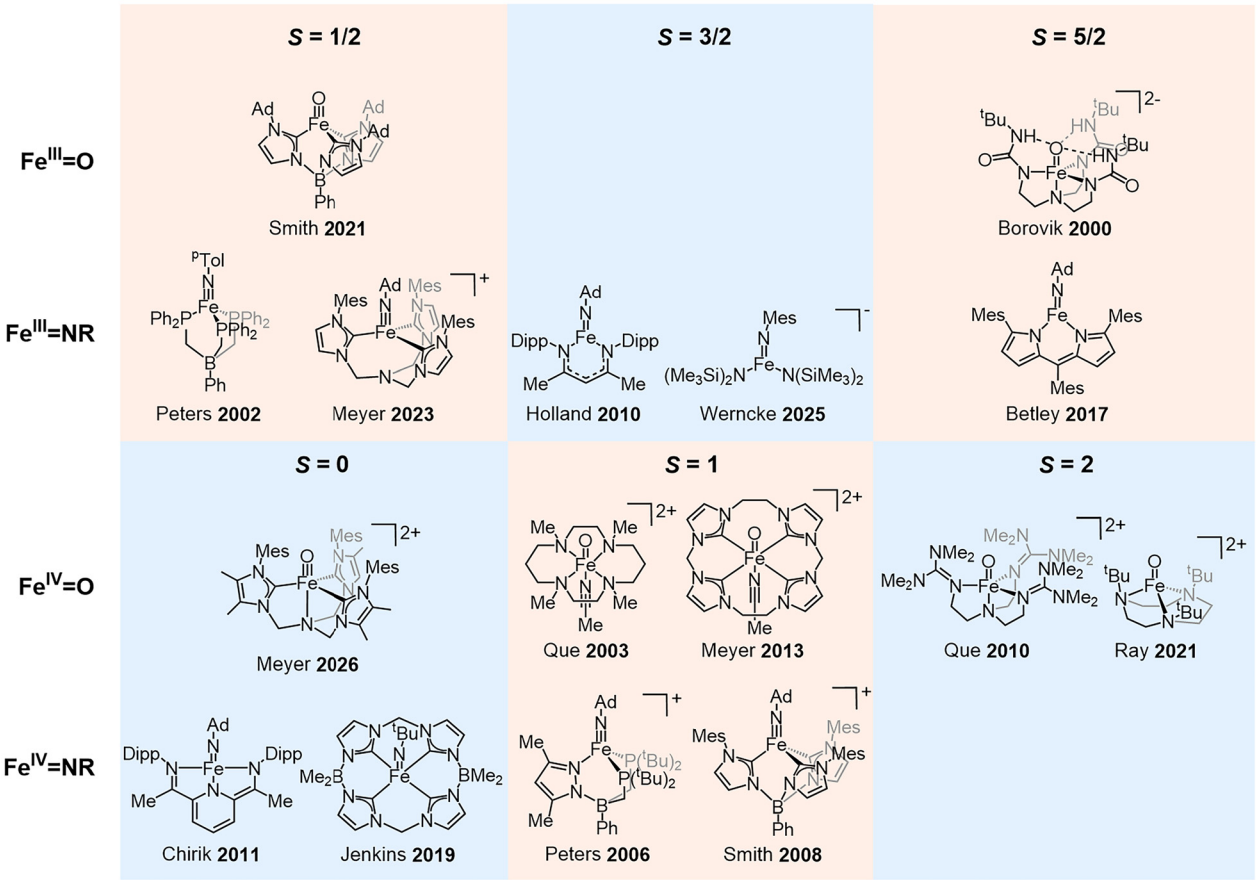

Fig. 1 Selected examples of molecular Fe(III)- and Fe(IV)-oxo and -imido intermediates organized by Fe oxidation states and ground spin states.[43–58]

electronic structure and reactivity. Such methods enable the elucidation of complex electronic structures and their relation to reaction mechanisms.[59] Application of computational methods also facilitates the interpretation of spectroscopic data, bridging theory and experiment.[59] Importantly, computational studies make it possible to investigate transient intermediates that cannot be isolated for direct experimental observation.[60] The most widely used electronic structure analysis method is density functional theory (DFT), due to its accuracy and relatively low computational cost. DFT is commonly applied to optimize geometries, explore molecular conformers and isomers, determine orbital occupations and energies, analyze excited states, calculate electronic spectra, and compute thermochemical corrections.[59]

DFT calculations have significantly contributed to the investigation of possible reaction mechanisms and reaction networks by locating reaction intermediates and transition states on the potential energy surface.[60] DFT analysis also allows computational evaluation of candidate catalysts, where calculated reaction barriers and related parameters can inform experimental catalyst design. However, DFT accuracy can be limited when applied on strongly correlated systems with degenerate orbitals, as is often seen with the d-orbitals and bond breaking and formation processes that occur during catalysis.[61,62] For these reasons, multireference wavefunction methods such as the complete active space self-consistent field (CASSCF)[63] method are widely used to provide more detailed descriptions of catalyst electronic structures. CASSCF calculations are typically followed by complete active space second-order perturbation theory (CASPT2)[64] or *N*-electron valence state perturbation theory (NEVPT2)[65] calculations to account for the missing dynamic correlation. Conventional CASSCF can typically only be used for an active space composed of up to 22 electrons occupying 22 orbitals, designated as CAS (22,22), due to the scaling of the CI vector as more configurations are added.[66] Often, larger active spaces beyond the current CASSCF limits are required to fully capture the electronic effects of a given catalyst, with one such example given in metalloporphyrins with extended π-systems. Common successful methodologies that allow extended active spaces are the full configuration interaction quantum Monte Carlo (FCIQMC), which uses Monte Carlo sampling to increase the size of the possible active spaces,[67] and the density matrix renormalization group (DMRG), which increases the size of the active space by considering the wavefunction as a matrix product state.[68–70] Both of these approaches enable efficient analysis of a catalyst's distal electronic features. For example, the π-system of an iron porphyrin complex has been analyzed using FCIQMC calculations with a CAS(40,38) active space and DMRG with a CAS(44,44) active space.[71,72] Coupled-cluster singles doubles and perturbative triples (CCSD(T)) is regarded as the gold standard in computational chemistry for calculating accurate energies for single-reference molecules. However, the exponential scaling of the method with respect to the number of basis functions makes it computationally prohibitive for most transition metal complexes. In recent years, the domain-based local pair natural orbital coupled cluster theory (DLPNO-CCSD(T)),[73] which exploits the locality of electron correlation to reduce the number of coupled-cluster amplitudes, has emerged as a viable method for calculating accurate energies, especially for cases where product selectivity is important.[74–77]

Even with these methodologies, it is not feasible to use quantum mechanics to study enzymes or other metalloproteins which can contain thousands of atoms. The quantum mechanics/molecular mechanics (QM/MM)[78,79] approach is commonly used for modeling enzymatic reactivity. In this framework, the metal center and its directly coordinated ligands are described with quantum-mechanical methods such as DFT or CASSCF, while the remainder of the protein environment and solvent are treated with classical molecular mechanics. QM/MM allows for the theoretical study of whole enzymes while retaining the accuracy of quantum mechanical calculations around the active site. While fundamentally different in scope and purpose, another emerging class of methods are the machine learning interatomic potentials (MLIPs) which offer a complementary route for accelerating quantum chemical calculations themselves.[80] These MLIP-based approaches have the potential to transform our ability to model complex reaction pathways with near-quantum accuracy at greatly reduced cost. However, their application to open-shell transition metal complexes with strong multiconfigurational character remains largely unexplored.[81]

While previous reviews have focused on the structures and reactivities of iron-oxo and iron-imido complexes, the explicit role of the σ- and π-channels as determinants of selectivity has not been systematically analyzed. Moreover, the influence of these channels in iron-imido complexes remains comparatively less explored than in iron-oxo systems. In this perspective, we explore how reaction channels influence product selectivity in well-known Fe(IV)-oxo intermediates and extend these insights to less common Fe(III)- and Fe(V)-oxo species. The reaction channels for iron-imido complexes have not been as well studied as for iron-oxo centers, resulting in limited data on their reactivity. Therefore, due to the isoelectronic nature between the two species, we treat the reaction channels for iron-imido complexes in comparison to the iron-oxo species and discuss how their reactivity may differ. We begin by briefly explaining the general aspects of the electronic structure of Fe (IV)-oxo and -imido intermediates before focusing on their chemistry and reaction channels. We examine how these factors influence the catalytic reactivities and selectivities of iron-oxo and iron-imido sites in both enzymatic and synthetic systems. The article concludes with a discussion on future work for the development of new iron-oxo and iron-imido catalysts based on these reaction channels for improved selectivity.

Discussion

The bonding of the iron-oxo and iron-imido in different coordination geometries has been explained in previous

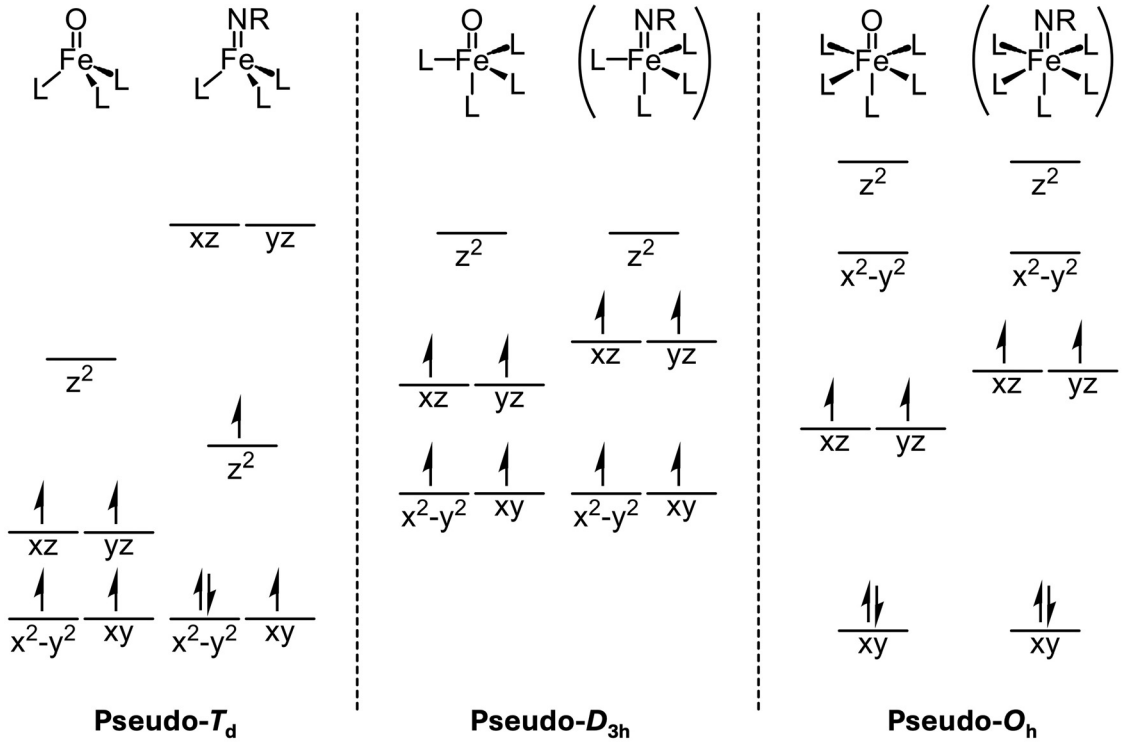

Fig. 2 Qualitative molecular orbital diagrams for an Fe(IV)-oxo and Fe(IV)-imido in pseudo-tetrahedral,[82–84] pseudo-trigonal bipyramidal,[85–87] and pseudo-octahedral coordination.[82,85,88] Geometries in parenthesis correspond to structures that have not been isolated and characterized.

reviews,[82,87,89] and we highlight the essential aspects here. Fig. 2 summarizes the d-orbital splitting across in the most common mode for Fe(IV)-oxo (*pseudo*-octahedral and -trigonal bipyramidal) and Fe(IV)-imido (*pseudo*-tetrahedral) intermediates.[82,83,89] For a *pseudo*-octahedral complex, the bonding of an iron-oxo involves the σ overlap of the metal d_{z^2} orbital with the oxygen $2p_z$ orbital and the π interaction between the d_{xz} and d_{yz} orbitals of the metal with the oxygen $2p_x$ and $2p_y$ orbitals. The metal $d_{x^2-y^2}$ orbital form σ bonds with the equatorial ligands and the d_{xy} exhibit nonbonding character. Typically, the d_{z^2} orbital is the highest in energy due to the strong antibonding character between the metal and the oxygen, unless the complex is surrounded by strong field equatorial ligands with a weak axial ligand.[88,90]

Due to their isoelectronic nature, iron-oxo and iron-imido intermediates have similar molecular orbital diagrams. Nitrogen 2p orbitals in iron-imido complexes are closer in energy to the d orbitals of the metal than oxygen 2p orbitals in iron-oxo complexes due to the smaller effective nuclear charge of nitrogen. Thus, the antibonding π* orbitals for iron-imido complexes are destabilized relative to iron-oxo complexes.[91] Due to this destabilization, the $d_{x^2-y^2}$ orbital can occasionally become lower in energy than the antibonding π* orbitals in a weak equatorial ligand field for an iron-imido complex.[92] Furthermore, while iron-oxo complexes typically have degenerate π* orbitals due to the symmetry of the iron-oxo, iron-imido geometry can be bent instead of linear, which leads to a breaking of the degeneracy of the π* orbitals. The nature of the R group of the imide also plays an important role in determining the electronic structure, as differing R groups can cause different spin states of iron complexes with the same auxiliary ligand.[37,51,93]

When iron-oxo/imido symmetry is reduced to *pseudo*-trigonal bipyramidal, the d_{xy} and the $d_{x^2-y^2}$ orbitals are both capable of bonding with the other equatorial ligands. This raises the energy of the d_{xy} orbital but lowers the energy of the $d_{x^2-y^2}$ orbital relative to *pseudo*-octahedral symmetry so that these two orbitals are degenerate. These are followed by the π* and σ* of the oxo/imide. In a *pseudo*-tetrahedral geometry, the d_{xy} and the $d_{x^2-y^2}$ orbitals both have nonbonding character. As well, the d_{z^2} orbital is lowered in energy due to mixing with the 4s and $4p_z$ orbitals of the metal which have the same symmetry, giving this orbital more nonbonding character.[94,95] The d_{xz} and d_{yz} orbitals can exhibit both σ* character with the ligands and π* character with the oxo/imido, further explaining the increase in energy of the π* orbitals compared to higher symmetry complexes.[96]

Reaction channels and electronic structure

Fe(IV) octahedral and trigonal bipyramidal complexes. Numerous studies have been carried out to understand the reactivity of iron-oxo species, especially for C–H bond activation with Fe(IV)-oxo species. In order for the initial hydrogen atom transfer (HAT) step of activating an alkane for hydroxylation to proceed, the Fe(IV)-oxo first adopts a radical Fe(III)-oxyl electron configuration upon elongation of the Fe–O bond by

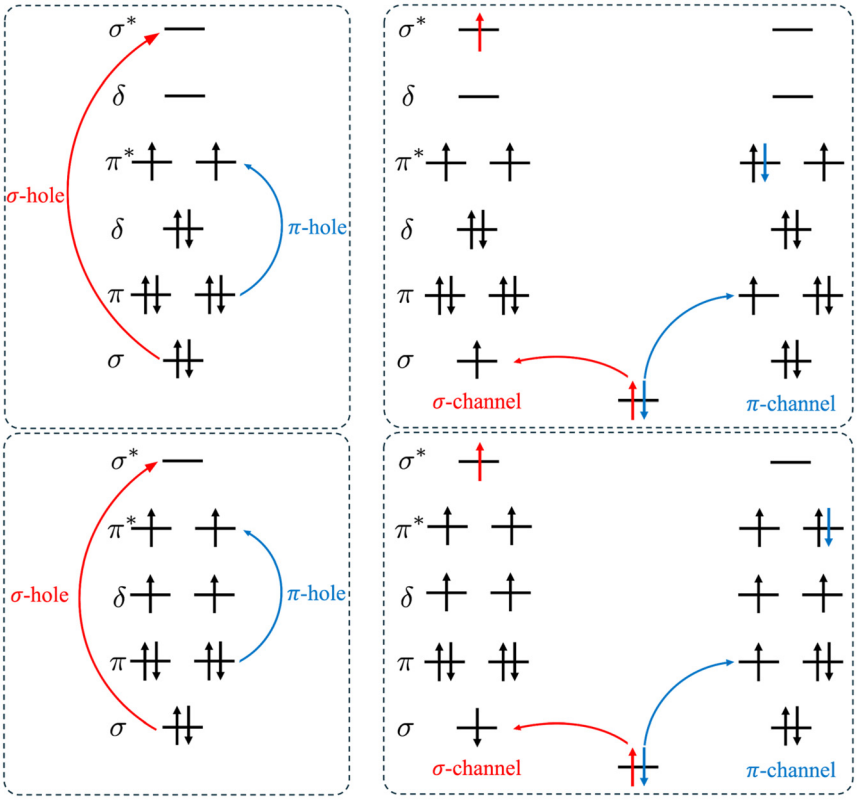

Fig. 3 Top, left: molecular orbital diagram of a S = 1 Fe(IV)-oxo or Fe(IV)-imido in a pseudo-octahedral environment showing the formation of the two different electron holes upon Fe–O bond elongation and reduction to Fe(III). Top, right: the corresponding molecular orbital diagram showing the two reaction channels for the transition state during hydrogen abstraction. Bottom, left: molecular orbital diagram of a S = 2 Fe(IV)-oxo or Fe(IV)-imido in a pseudo-trigonal bipyramidal environment showing the formation of the two different electron holes upon bond elongation and reduction to Fe(III). Bottom, right: the corresponding molecular orbital diagram showing the two reaction channels for the transition state during hydrogen abstraction.

electron transfer from the ligand-based bonding orbitals to the metal-centered antibonding orbitals (Fig. 3).[97] There are two possible channels for the adoption of radical character, creating either a π-hole or a σ-hole depending on which orbital an electron is excited from.[97] To create the π-hole, an electron is promoted from the π orbitals to the π* orbitals, and for a σ-hole, an electron is excited from the Fe–O σ orbital to the σ* orbital (Fig. 3).[98] This transition can account for most of the energy apparent in the reaction barrier.[99] The $d_{x^2-y^2}$ and d_{xy} orbitals are not involved in these channels as they cannot interact with the substrate.

After formation of the Fe(III)-oxyl intermediate, an electron is added from the substrate to the now singly occupied σ orbital in the σ-channel or the singly occupied π orbital in the π-channel during the HAT step.[97] Synthetic Fe(IV)-oxo intermediates are typically found in two possible spin states in two different coordination environments, triplet in a tetragonal geometry or quintet in a *pseudo*-trigonal bipyramidal geometry. For each spin state, there is theoretically both σ- and π-channels available which leads to four main reaction channels (Fig. 3).[100,101] Typically, the lowest energy channel is the σ-channel for quintets and the π-channel for triplets.[100] The quintet π-channel is energetically comparable to the triplet π-channel with the triplet σ-channel much higher in energy due to occupying a high energy orbital.[100] However, the triplet π-channel can sometimes be lower in energy than the quintet σ.[102] The low energy of the quintet σ-pathway is due to the gain of exchange from promoting an electron to an unoccupied orbital. The availability of the quintet π-channel, despite the loss of exchange, is due to high covalency of the Fe–O π bond.[103] If the $d_{x^2-y^2}$ orbital is destabilized relative to the σ* orbital, such as through the use of stronger-field equatorial ligands or if the d_{z^2} is stabilized by weakening or removing the axial ligand *trans* to the oxo, the system can access the triplet σ-channel.[90]

The reaction channels have an effect on the geometry of the transition state to increase overlap with the appropriate orbital, as the π-channel will exhibit an Fe–O–H bond angle around 120° whereas the σ-channel will be almost colinear.[97,100] These channels explain in part why synthetic triplet iron-oxo catalysts often exhibit two-state reactivity, where the HAT step proceeds through a quintet transition state. The π-channel is usually sterically hindered and so the σ-channel on the quintet pathway is the only energetically accessible pathway.[97] Understanding these reaction channels also provides key insights into the diverse reactivities exhibited by

iron-oxo catalysts. For instance, triplet complexes with a π-channel sterically blocked leave only the σ-channel accessible to the substrate and consequently, exhibit higher activation barriers than those with an open π-channel. This is because accessing the σ-channel requires promoting an electron into the higher-energy σ* orbital, incurring a greater energy penalty.[104] Since both reaction channels require populating high energy antibonding orbitals, their relative energies between these orbitals (most notably the σ* orbital due to its high energy) strongly influence reactivity. Lowering the energies of these antibonding orbitals facilitates access to the corresponding quintet transition states, thereby enabling more reactive catalysts.[105] Sautet and coworkers reported a linear relationship between the computed reaction barrier for C–H hydroxylation of methane and the energies of the σ*/π* orbitals for high-spin and low-spin iron-oxo complexes, respectively.[105] It has also been shown computationally that Fe(III)-oxyl formation is easier with weak-field ligands than with strong-field ligands.[101] Additional experimental and computational analyses support these findings and show that weaker-field ligands result in lower reaction barriers.[105–110] Structural changes to the ligand which result in a weaker ligand field, such as distortions due to steric effects, also lower reaction barriers and increase reactivities.[111,112] Complexes with greater oxyl character in the Fe(IV)-oxo intermediate are more reactive towards C–H bond activation as less energy is required to create the Fe(III)-oxyl.[113,114]

Iron-imido complexes are isoelectronic to the related iron-oxo complexes. Their valence orbital similarities are evidenced by the HAT efficacies of iron-imido intermediates in C–H activation reactions which proceed *via* mechanisms similar to those of iron-oxo species. Many of the same mechanistic principles apply, although iron-imido systems have been less extensively studied. Like iron-oxo species, iron-imido complexes exhibit higher reactivities towards C–H bond activation upon reduction to their Fe(III)-imidyl forms.[115,116] Iron-imido intermediates bear an additional substituent on the imide nitrogen relative to the iron-oxo, and this can have a profound impact on both reactivity and reaction channel preference. While iron-oxo complexes can react *via* σ- and π-channels, many iron-imido species can only react through the π-channel due to the steric bulk of the imido R group blocking colinear σ-attack between the alkane and the imide.[117] Additionally, Fe(IV)–NTs (NTs = tosylimido) complexes accept electrons from substrates at a greater distance than its iron-oxo analogue due to the iron-imido having a greater electron affinity than the iron-oxo.[118] Therefore, within iron-imido-catalyzed C–H activation reactions, the active species is the less reactive Fe(III)-imide which is formed upon substrate HAT. These two factors explain the inert character of some iron-imido complexes towards C–H bond activation compared to the related iron-oxo complexes,[118] although the increased electron accepting distance for iron-imido complexes can also relieve steric strain when oxidizing bulky substrates or when surrounded by a bulky ligand. One such Fe(IV)–NTs complex was found to be more reactive than its oxo counterpart towards C–H activation of thioanisole and the related iron-oxo complex being more reactive towards less bulky substrates due to its longer Fe–N bond making the σ-channel more accessible for bulky substrates compared to the iron-oxo.[119]

Besides blocking the σ-channel, the substituent of the imide can affect the reaction channels in more subtle ways. As previously mentioned, the substituent can impact the spin state of the complex. As the prevailing channel is influenced by the spin state of the complex, careful tuning of the nature of the substituent could be used to control which reaction channel is dominant. Similarly, for a recent *pseudo*-trigonal planar Fe(IV)–bisimido complex, electron donating groups on the imide were found to control both the spin state and if the reaction proceeded through alpha spin transfer or beta spin transfer during hydrogen abstraction.[37] The beta electron transfer was blocked for one of the complexes, as the singly occupied orbitals were rendered as non-bonding instead of having π* character due to the loss of covalency of the Fe–N bond caused by the electron withdrawing groups on the imide.[37] The ability to use substituents to control the mechanism for electron transfer could be influential in controlling the prevailing reaction pathway in low coordinate iron-imides.

Fe(IV) tetrahedral. Due to the numerous Fe(IV)-oxo complexes that exist with four and five coordinate ligands, most analysis has been centered on these geometries. *Pseudo*-tetrahedral Fe(IV)-oxo complexes, while rare, have been reported or studied computationally in every accessible spin state, S = 0, 1, and 2.[56,120,121] A study of these reaction channels for the singlet structure reveals that these iron-oxo complexes affect substrate oxidation through the quintet transition state and thus prefer the σ-channel for both epoxidation and hydroxylation.[83] C–H hydroxylation *via* a triplet spin complex proceeds *via* the quintet spin state as well, similar to the two-state reactivity known for octahedral complexes.[121,122] Therefore, the π-channel might be inaccessible due to the high energy of the π* orbitals compared to the σ* orbital (Fig. 2), although further studies on additional structures are required to confirm which pathways are accessible. While the iron-imido is found in a four-fold coordinate environment much more commonly than the iron-oxo (Fig. 1), the σ- and π-channels for this species have not been examined.

Fe(V) complexes. While most of the discussion so far has been limited to Fe(IV) cases, we can extend this framework to understand the reactivities of Fe(V) and Fe(III) species. There are only a few studies which reported examining the two reaction channels for these oxidation states for iron-oxo complexes, and none for iron-imido species. Iron exists as a d^3 metal in Fe(V)-oxo and Fe(V)-imido complexes, thus, the only available spin states are doublet and quartet. It is possible to have one singly occupied and one empty π* orbital in the doublet, or two singly occupied π* orbitals for the quartet in a *pseudo*-octahedral environment. Accordingly, the σ-channel is likely inaccessible, in contrast to the S = 1 tetragonal Fe(IV)-oxo cases. HAT is therefore expected to proceed *via* the π-channel, as suggested by Ansari and coworkers.[123,124] However, a detailed assessment of σ-channel accessibility, spin state

effects in Fe(v)-oxo intermediates, and the role of geometric variations remains lacking. However, these reaction channels have been studied in Mn(iv)-oxo analogues, which are isoelectronic to the Fe(v)-oxo, since both compounds exhibit a d^3 configuration. Similarly to the $S = 1$ iron-oxo, C–H activation reactions with manganese-oxo catalysts proceed through the π-channel as the σ* orbital is too high in energy to favor the formation of the oxyl,[125] even for quartet systems.[87] To access the σ-channel, it is likely that the geometry must be reduced to *pseudo*-tetrahedral, as this can allow for an energetically available σ* orbital (Fig. 2), although these geometries are likely only possible for Fe(v)-imides given the lack of low coordinate iron-oxo species and the high oxidation state of iron. In higher coordination environments, an Fe(v) complex would most likely have an empty π* or nonbonding orbital compared to Fe (iv) which would be more favored to accept an electron than the higher energy σ*, although further examination is required to confirm if this is true.

Although Fe(v)-imido complexes are sparse, several systems provide useful precedent for their electronic structure. Relevant precedent comes from a TAML-supported Fe(v)-imido complex, featuring a bent Fe–N–S motif that increases σ-bond character in the Fe–N interaction relative to the linear Fe–N–S motif observed for the related Fe(iv)-imido.[126] The Fe(v)-imido TAML complex affects nitrene transfer for thioether substrates, but HAT reactivity toward amine products is observed for saturated hydrocarbon substrates.[126] Because the σ* orbital is expected to be energetically inaccessible, both transformations would be predicted to proceed through a π-type pathway. It may be possible that Fe(v)-imido ligand fields could reduce σ* orbital energies enough to allow access to σ-channel pathways in Fe(v) systems, although this possibility has yet to be demonstrated experimentally. Furthermore, comparisons of Fe(iv)-imido and Fe(iv)-oxo complexes demonstrate that Fe(iv)-imido donors alter the frontier molecular orbitals relative to oxo analogues by breaking the degeneracy of the π* orbitals.[127] This results in selective stabilization of one π* orbital and destabilization of the other, increasing the overall σ-donation of the imido ligand relative to the corresponding Fe(iv)-oxo.[127] This difference enhances electron-transfer reactivity at Fe(iv) and provides a useful precedent for anticipating comparable electronic effects in Fe(v)-imido species.

Fe(iii) complexes. A similar analysis can be extended to Fe (iii)-oxo intermediates, although such species are considerably less common than their Fe(v)-oxo counterparts. A sextet Fe(iii)-oxo N4Py complex was recently examined and compared to its Fe(iv) analogue in C–H activation reactions.[128] As the sextet spin state is a high-spin d^5 metal, all the d orbitals are already singly occupied which renders excitation to the high-energy σ* energy unfeasible. Here, instead of undergoing the formation of the Fe(ii)-oxyl concurrent with substrate HAT, a proton coupled electron transfer (PCET) mechanism is suggested where an electron is transferred to the metal and the substrate hydrogen atom is transferred to the oxygen.[128] A similar PCET mechanism was observed in Borovik's Fe(iii)-oxo complex.[48] This C–H activation mechanism is uniquely different than a typical HAT mechanism, in which both electrons are transferred to the oxygen.[128] The quartet spin state is capable of affecting HAT *via* the σ-channel due to the unoccupied σ* orbital.[128] A doublet Fe(iii)-oxo would have one doubly occupied and one singly occupied π* orbital so, as for the low-spin Fe(iv)-oxo, the σ-channel is likely not available in a *pseudo*-octahedral environment. A doublet *pseudo*-T_d Fe(iii)-oxo was found to proceed through the $^4\sigma$ channel for HAT.[121] However, hydroxyl rebound was found to not be accessible for this Fe(iii) complex due to the low electron affinity of the Fe(ii)-hydroxyl to form the Fe(i) complex.[121] This explains why the complex could only perform dehydrogenation of ethylbenzene instead of hydroxylation or epoxidation.[43] Therefore, Fe(iii) species might struggle to be effective catalysts for oxidation reactions.

As with the Fe(iii)-oxo, we can look at the isoelectronic d^5 Co(iv)-oxo to gain more information about possible reaction channels. C–H activation reactions with both a doublet and sextet *pseudo*-O_h Co(iv)-oxo proceed along the π-channel, confirming our speculation above.[76,129] We were not able to identify any reported Co(iv)-oxo species in the quartet state to confirm if they proceed by the σ-channel instead. A summary of which reaction channels have been observed in different geometries, spin states, and oxidation states, is given in Table 1.

Table 1 Reported reaction pathways for iron-oxo and -imido complexes in different oxidation states, spin states, and molecular geometries (pseudo-octahedral, pseudo-trigonal bipyramidal, and pseudo-tetrahedral). Ligand field strength, iron spin state, and/or substrate orientation may also provide access to both σ- and π-channels. Reaction channels confirmed by both experiment and computation are shown in bold font;[90,100,102,103,130–135] channels supported solely by computational studies[83,121,123,124,128,136] are shown in regular font

	Fe^{III}	Fe^{IV}	Fe^{V}
O_h	$^4\sigma$, $^6\pi$	$^3\boldsymbol{\sigma}$, $^3\boldsymbol{\pi}$ $^5\boldsymbol{\sigma}$, $^5\boldsymbol{\pi}$	$^2\pi$, $^4\pi$
D_{3h} [a]	—	$^5\boldsymbol{\sigma}$, $^5\boldsymbol{\pi}$	—
T_d [a]	$^2\pi$, $^4\sigma$	$^5\sigma$, $^5\pi$	—

[a] The molecular orbital diagram in Fig. 2 is considered but the relative energies of the π* orbitals can change for C_{3v} geometries depending on ligand field strength.

Reaction channels and product selectivity

While these channels have mostly been studied in the context of C–H bond activation, they are also applicable to other chemical reactions involving an Fe(iv)-oxo or -imido intermediate. We have previously applied these concepts to $C_2 + N_1$ alkene aziridination reactions with macrocyclic Fe(ii) tetracarbene catalysts. We found that in the transition state for alkene addition to the Fe(iv)-imido, there are two channels available. One channel involves addition of an alpha electron to the σ orbital between iron center and the imide nitrogen, while the other channel involves beta electron addition to one of the π orbitals between the iron center and the imide nitrogen. These results suggest that in the σ-channel, the radical is antiferro-

magnetically coupled to the iron-imido and in the π-channel the radical is ferromagnetically coupled. The σ-channel was found to be preferred for the $S = 1$ macrocyclic Fe(II) tetracarbene complexes. For macrocyclic Fe(II) tetracarbenes, the σ* orbital is typically below the $d_{x^2-y^2}$ orbital due to the strong equatorial ligand field and the lack of an axial ligand. For this reason, the σ-channel is not likely to be as favored for other triplet aziridination catalysts. We then considered the HOMO–LUMO gap between the π* and the σ* orbitals of the imide intermediate as a descriptor for the catalytic activity of the σ-mechanism as it influences the availability of the σ-channel over the π-channel.[137]

The σ- and π-reaction channels analyzed in the previous section can profoundly influence ligand design for development of catalysts that favor specific products, and some representative examples are summarized in Scheme 1. Although C–H hydroxylation is typically affected by iron-oxo catalysts which favor the σ-channel (reactive high-spin enzymes and catalysts), alternative reaction channels can be selectively promoted under appropriate conditions. C–H hydroxylation typically proceeds along the σ-channel, so enzymes that catalyze alternative reactions often orient the substrate to favor the π-channel due to longer OH rebound allowing the resulting radical species to react with other species.[138,139] This has been further enforced as mutations to hydroxylase enzymes which enforce strict π-channel reactivity. Iron-oxo catalysts like these typically have higher reaction barriers towards HAT than those which prefer the σ-channel.[140,141] Additionally, in enzymes, almost linear Fe–O–H bond angles are known to correspond to C–H hydroxylation selectivity while acute Fe–O–H bond angles suggest alternative reactivity due to these intermediates' preferences for the σ- and π-channels, respectively.[142] To highlight differences between σ- and π-channel reactivity in catalytic transformations, Scheme 1 provides relevant examples for which different channels give distinct products in enzymatic and synthetic iron systems.

These examples evince how controlling access to the σ- and π-channels can guide catalyst design in Fe(IV)-oxo and Fe(IV)-imido systems. For C–H activation, catalysts that stabilize or enable the σ-channel tend to favor hydroxylation and amination pathways, whereas restricting σ-channel access can promote epoxidation, halogenation, and nitrene transfer reactions in systems where rebound is disfavored. Thus, differentiation of structural features including ligand donor strength, symmetry, steric access, and substrate positioning provides a framework for tuning σ/π-channel availability. These principles also suggest opportunities for directing reactivity in high-valent Fe(III)- and Fe(V)-imido platforms and may extend to Mn-, Co-, and Ru-based oxo and imido systems, where similar considerations of orbital alignment and substrate approach geometry govern product selectivity.

The use of the π-channel for forming non-hydroxylated products has been most widely studied for halogenation with Fe(IV)-oxo containing halogenase enzymes. Substrate orientation has long been known to control the selectivity of halogenation over hydroxylation in enzymes like SyrB2 and WeI2O5.[147,148] It was ultimately found that the selectivity was related to the availability of the σ- and π-channels, with hydroxylases favoring the σ-channel and halogenases the π-channel.[138,143] The π-channel is preferred for halogenation for many reasons. In SyrB2 C–H activation systems, there is a rehybridization of the Fe–Cl π* orbital that is not observed for the Fe–OH π* orbital which allows for better overlap with the substrate.[138] Although the π-channel is theoretically higher in energy than the σ-channel, the π-channel is stabilized as the π* orbital exhibits more oxyl character than the σ* orbital, resulting in better overlap with the substrate and an earlier transition state as the orbital is polarized more towards oxygen.[134] Additionally, at bond distances corresponding to transition state bonding (~1.8 Å), the d_{xz} orbital is stabilized and exhibits greater oxyl character due to π anisotropy.[135] This analysis can also be extended to explain the reactivity in other enzymes. Recently, a homologue of the cyclopropanase enzyme HrmJ was found to instead affect C–H hydroxylation with 6-nitronorleucine.[144] A slight change in the substrate orientation enhanced the availability of the σ-channel over the π-channel, resulting in enzymatic hydroxylation instead of cycloproponation.[144]

While many studies rely on just the angle between iron, oxygen, and the substrate to determine the reaction channel, this metric might not be sufficient to accurately determine reaction channel preference. One study comparing halogenases and hydroxylases found that when the bond angle of the substrate is adjusted to match that of the other reaction channel, hydroxylases do not access the π-channel and halogenases do not access the σ-channel.[148] Similarly, Ahsan *et al.* found that for similar pathways, relevant bond angles that would typically be matched to the π-channel instead corresponded to the σ-channel.[149] Additionally, these angle values changed substantially depending on the choice of dispersion correction and solvation.[149] Therefore, studying bonding geometry alone is not enough to definitively determine the prevailing reaction channel. It is necessary to understand the electronic structure and see which orbitals are involved in the transition state. Furthermore, while this mechanism works well to describe the selectivity for halogenases, it is less clear how much of an impact it has for enzymatic selectivity for other reactions. Among catalytic epoxidation reactions, the σ-channel is associated with C–H hydroxylation, whereas the π-channel is associated with alkene epoxidation.[142,150] A recent study suggests that unlike halogenation reactions, which feature a halogen atom that readily accepts the resulting substrate radical, π-channel preference alone is not enough to explain why the substrate does not undergo hydroxyl rebound.[145] While the reaction channels do give rise to the expected products, other factors such as interaction with adjacent residues are important in stabilizing the radical to ensure it forms an epoxide instead of undergoing hydroxyl rebound.[145]

These reaction channels can also control chemoselectivity within the same reaction. When treated with (4-hydroxyphenol)pyruvate, the enzyme HmaS selectively activates benzylic C–H bonds for benzyl alcohol products whereas the enzyme HPPD favored arene C–H activation and gave the related

Catalyst	Substrate	σ Product	π Product	Ref.
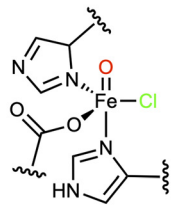 $[Fe^{IV}=O(SyrB2)]^0$	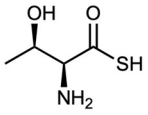	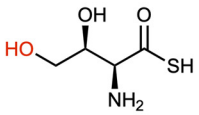	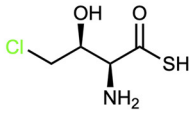	137 and 142
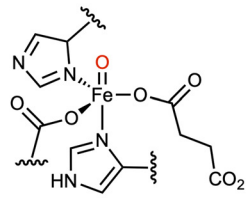 $[Fe^{IV}=O(HrmJ)]^0$	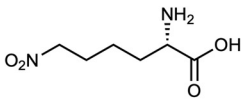	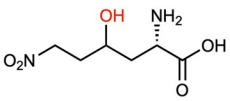	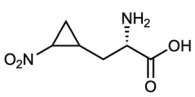	143
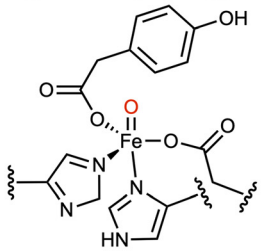 $[Fe^{IV}=O(Hmas/HPPD)]^0$	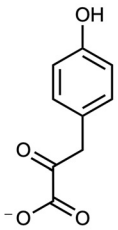	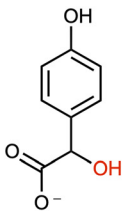	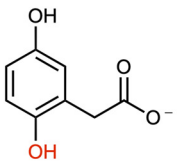	130
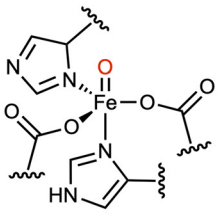 $[Fe^{IV}=O(H6H)]^0$	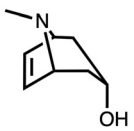	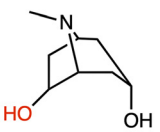	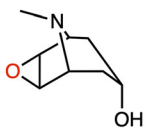	144
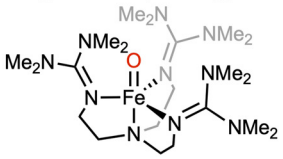 $[Fe^{IV}=O(TMG_3Tren)]^{2+}$		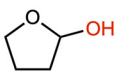	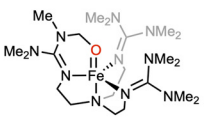	55 and 132
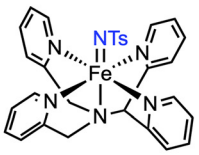  $[Fe^{IV}=NTs(N4Py)]^{2+}$		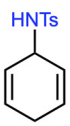		116 and 145

Scheme 1 Examples of Fe(IV)-oxo and Fe(IV)-imido intermediates that have different products for the σ-channel and the π-channel for both enzymes and synthetic systems

phenol products. These enzymes have the same primary coordination sphere; only the orientation of the pyruvate ring is different between them. The difference in reactivity is rooted in the availabilities of the σ- and π-channels, as HPPD proceeds through the σ-channel and HmaS through the π-channel.[131] This difference in reactivity is due to substrate alignment. Benzylic carbons can only bind with iron-oxo oxygen atoms in the vertical position relative to iron, favoring

σ-orbital overlap, but the arene carbon atoms of the pyruvate favor π* orbital overlap.[131] Here the differing spin states, due to antiferromagnetic or ferromagnetic coupling of the resulting radical with the iron center, also resulted in a geometry change in the transition state.[131] The high spin σ-channel adopted a *pseudo*-trigonal bipyramidal geometry, and the intermediate spin π-channel adopted a *pseudo*-square planar geometry, which also affects the overlap of the substrate with the relevant iron-oxo orbitals.[131]

While these reaction channels are well known in metalloenzymes, they also play an important role in synthetic Fe(IV)-oxo complexes. The π-channel could be used to favor alkene epoxidation over C–H hydroxylation. Preference for the π-channel for alkene epoxidation over C–H hydroxylation was observed by Bhardwaj and Mondal for a singlet, *pseudo*-tetrahedral iron-oxo complex with cyclohexadiene, although the σ-channel again had lower total barriers for both reactions.[83] Therefore, increasing the availability of the π-channel should improve selectivity for epoxidation over hydroxylation. The π-channel is not always available in synthetic systems, however. Costas and Roithová found that for $[Fe(IV)=O(PyTACN)Cl]^+$ complexes, the triplet state has significantly higher energy barriers for epoxidation reactions of cyclohexene over hydroxylation than in the quintet state, likely related to π- or σ-channel preference. Formation of the triplet state intermediate is expected to proceed through the π-channel, which requires a more acute Fe–O–H bond angle and closer substrate proximity than the quintet σ-channel. The smaller bond angle results in a significantly higher energy barrier to alkene C=C activation than hydrogen abstraction due to steric hindrance and thus the π-channel is favored.[13] Therefore, it is important that the π-channel is not sterically hindered in order to promote catalytic epoxidation over hydroxylation.

We should also highlight that in iron-oxo molecular complexes, the π-pathway does not always lead to desirable products, since it can result in the deactivation of the catalyst. One illustrative example is the TMG_3tren iron-oxo complex, which is capable of undergoing self-oxidation.[55] Subsequent computational analysis suggested C–H bond activation to proceed through the σ-channel and ligand oxidation through the π-channel.[133] Because the ligand's hydrogen atoms are pointing towards the Fe–O axis, they are directly positioned next to the π orbital with predominant p_x/p_y character of the oxo/oxyl.[133] Similarly, N4Py iron-oxo derivatives with aryl substituents near the oxo moiety are also known to undergo ligand oxidation which proceeds through the π-channel.[102,151]

While the reaction channels have already been exploited readily to control selectivity in iron-oxo intermediates, especially in metalloenzymes, there has been less focus on applications towards catalytic nitrene transfer reactions with iron-imido catalysts. As mentioned earlier, if the σ-channel is blocked for iron-imides due to steric bulk from the imide substituent, different reactions than C–H amination are preferred. For example, the availability of the σ- and π-channels explains why Fe-NTs N4Py complexes have lower barriers towards sulfoxidation of dimethyl sulfide than hydroxylation of cyclohexadiene, while the iron-oxo, which does not have a blocked σ-channel, exhibits lower barriers for hydroxylation over sulfoxidation.[146] Therefore, a less sterically demanding imido ligand that enables access to the σ-channel would be expected to favor amination over sulfoxidation in Fe(IV)-imido species. Similarly, for a TPA iron-imido catalyst, the Fe(IV)=NTs complex, which can only react *via* the π-channel, was found to be a stronger oxidant than the TPA Fe(IV)-oxo towards ligand oxidation.[152] The σ-channel is typically unavailable during ligand oxidation reactions due to the ligand not being able to achieve a colinear approach, and this results in greater oxidative strength for the Fe(IV)-imide than the Fe(IV)-oxo.[117] Because the σ-channel is rendered inaccessible by the imide, it should be possible to greatly improve selectivity for iron-imido catalysts. Unlike the related iron-oxo catalysts, for iron-imido catalysts the π-channel, which leads to non-amine products, is often preferred. Similarly, for designing enhanced C–H amination catalysts, it might be necessary to utilize smaller imide nitrogen substituents that do not hinder the availability of the σ-channel for improved selectivity towards C–H bond activation.

Conclusions and Outlook

The σ- and π-channels have a significant impact on the chemoselectivity of Fe(IV)-oxo intermediates in enzymes and their biomimetic analogues. While there has been extensive work on understanding these reaction pathways for Fe(IV)-oxo species, especially for enzymatic halogenation, significantly more work is needed to understand these reaction channels for other reactions. Most studies have focused on the reaction channels for Fe(IV)-oxo complexes with *pseudo*-octahedral and *pseudo*-trigonal bipyramidal ligands, but, in contrast, most iron-imido species exhibit lower coordinate geometries. Therefore, the study of different molecular geometries is vital for controlling selectivity in catalytic iron-imido reactions. Additionally, the selectivity of Fe(V)- and Fe(III)-oxo intermediates relating to these channels is not well understood, and the study of related iron-imido species in differing oxidation states is non-existent. Iron-oxo intermediates of different oxidation states than Fe(IV) could be promising catalysts for non-hydroxylation reactions due to strict π-channel preferences reported so far for these complexes. Utilization of competent iron-imido intermediates offers a unique opportunity to exploit this selectivity, since the σ-channel, which favors C–H amination, can be blocked by selecting appropriate bulky R groups of the imide.

These pathways can also be exploited in synthetic catalytic systems. As C–H bond activation favors the σ-channel, ensuring this pathway is readily accessible will help improve hydroxylation and amination catalysts. Catalytic amination can be enhanced through understanding how the substituent attached to the imide and the substrates employed block σ-channel access, which increases the hydrogen abstraction barrier. Catalytic epoxidation/aziridination and halogenation reactions, as well as other reactions that rely on avoiding hydroxyl rebound, can benefit from further studies on how to

block the σ-channel to exploit the benefits seen in enzymatic systems. Additionally, the study of lower coordination environments for Fe(III)- and Fe(V)-oxo and -imido intermediates may elucidate more cases in which the pathway of interest can be controlled. Understanding the reactivity channels of these systems could help improve product selectivity over hydroxylation and amination due to the preference for the π-channel observed thus far for Fe(V)-oxo and Fe(IV)-imido species.

While traditional catalyst design relies on experimental methods or *in silico* high throughput screening using conventional computation methods, these techniques are monetarily or temporally prohibitive and limited to small databases. The rise of artificial intelligence (AI) in recent years has allowed for the rapid exploration of broad chemical spaces for the development of novel catalysts.[81] Several studies have applied machine learning to ligand design for iron-oxo catalysts,[153–155] but these efforts have primarily focused on Fe(IV)-oxo species involving C–H hydroxylation reactions. The chemical space for additional catalytic reactions, like C–H halogenation or alkene epoxidation, as well as other highly reactive candidate catalysts, such as Fe(V)-oxo or the Fe(IV)-imido complexes, remains largely unexplored making it an encouraging avenue and worthy pursuit for future research. To unlock the full potential of AI-driven catalyst design, future machine learning workflows must integrate mechanistic understanding, such as the reaction channels and electronic structure considerations highlighted here, into their modeling frameworks. Incorporating these details will allow for more faithful representations of metal-oxo and metal-imide complexes and ultimately drive more transformative advances in reactivity and design.

Conflicts of interest

The authors declare no competing financial interest.

Data availability

No new experimental or computational work was performed for this work and no new results are presented here.

Acknowledgements

This work was supported by the National Science Foundation under Grant CHE 2154697. Any opinions, findings, and conclusions expressed in this material are those of the authors and do not necessarily reflect the views of the National Science Foundation.

References

1 R. Ushimaru and I. Abe, *ACS Catal.*, 2023, **13**, 1045–1076.
2 J. Hohenberger, K. Ray and K. Meyer, *Nat. Commun.*, 2012, **3**, 720.
3 E. L. Hegg and L. Que Jr, *Eur. J. Biochem.*, 1997, **250**, 625–629.
4 E. I. Solomon, S. Goudarzi and K. D. Sutherlin, *Biochemistry*, 2016, **55**, 6363–6374.
5 J. C. Price, E. W. Barr, B. Tirupati, J. M. Bollinger and C. Krebs, *Biochemistry*, 2003, **42**, 7497–7508.
6 L. M. Hoffart, E. W. Barr, R. B. Guyer, J. M. Bollinger and C. Krebs, *Proc. Natl. Acad. Sci. U. S. A.*, 2006, **103**, 14738–14743.
7 B. E. Eser, E. W. Barr, P. A. Frantom, L. Saleh, J. M. Bollinger Jr, C. Krebs and P. F. Fitzpatrick, *J. Am. Chem. Soc.*, 2007, **129**, 11334–11335.
8 D. G. Fujimori, E. W. Barr, M. L. Matthews, G. M. Koch, J. R. Yonce, C. T. Walsh, J. M. Bollinger Jr, C. Krebs and P. J. Riggs-Gelasco, *J. Am. Chem. Soc.*, 2007, **129**, 13408–13409.
9 M. Guo, T. Corona, K. Ray and W. Nam, *ACS Cent. Sci.*, 2019, **5**, 13–28.
10 H. Song, N. Naowarojna, R. Cheng, J. Lopez and P. Liu, in *Advances in Protein Chemistry and Structural Biology*, ed. T. Karabencheva-Christova and C. Z. Christov, Academic Press, 2019, vol. 117, pp. 1–61.
11 C. Krebs, D. G. Fujimori, C. T. Walsh and J. M. Bollinger Jr, *Acc. Chem. Res.*, 2007, **40**, 484–492.
12 L. Roy, *ChemPlusChem*, 2019, **84**, 893–906.
13 T. Terencio, E. Andris, I. Gamba, M. Srnec, M. Costas and J. Roithová, *J. Am. Soc. Mass Spectrom.*, 2019, **30**, 1923–1933.
14 E. F. Gérard, V. Yadav, D. P. Goldberg and S. P. de Visser, *J. Am. Chem. Soc.*, 2022, **144**, 10752–10767.
15 T. M. Buscagan and D. C. Rees, *Joule*, 2019, **3**, 2662–2678.
16 E. I. Solomon, A. Decker and N. Lehnert, *Proc. Natl. Acad. Sci. U. S. A.*, 2003, **100**, 3589–3594.
17 F. Tavani, G. Capocasa, A. Martini, F. Sessa, S. Di Stefano, O. Lanzalunga and P. D'Angelo, *Phys. Chem. Chem. Phys.*, 2021, **23**, 1188–1196.
18 D. Kumar, H. Hirao, L. Que and S. Shaik, *J. Am. Chem. Soc.*, 2005, **127**, 8026–8027.
19 J. Lin, Q. Sun and W. Sun, *RSC Adv.*, 2021, **11**, 2293–2297.
20 Y. Sheng, C. S. Abelson, J. Prakash, A. Draksharapu, V. G. Young Jr and L. Que Jr, *Angew. Chem., Int. Ed.*, 2021, **60**, 20991–20998.
21 O. Cussó, M. Cianfanelli, X. Ribas, R. J. M. Klein Gebbink and M. Costas, *J. Am. Chem. Soc.*, 2016, **138**, 2732–2738.
22 B. Chandra, F. Ahsan, Y. Sheng, M. Swart and L. Que, *Proc. Natl. Acad. Sci. U. S. A.*, 2024, **121**, e2319799121.
23 X. Engelmann, D. D. Malik, T. Corona, K. Warm, E. R. Farquhar, M. Swart, W. Nam and K. Ray, *Angew. Chem., Int. Ed.*, 2019, **58**, 4012–4016.
24 K. M. Blatchford, V. H. Stafford III, T. D. Jones, K. D. Vogiatzis and D. M. Jenkins, *Organometallics*, 2025, **44**, 1304–1313.
25 T. Kojima, R. A. Leising, S. Yan and L. Que Jr, *J. Am. Chem. Soc.*, 1993, **115**, 11328–11335.
26 P. Comba and S. Wunderlich, *Chem. – Eur. J.*, 2010, **16**, 7293–7299.

27 O. Planas, M. Clémancey, J.-M. Latour, A. Company and M. Costas, *Chem. Commun.*, 2014, **50**, 10887–10890.
28 M. Puri, A. N. Biswas, R. Fan, Y. Guo and L. Que Jr, *J. Am. Chem. Soc.*, 2016, **138**, 2484–2487.
29 S. Rana, J. P. Biswas, A. Sen, M. Clémancey, G. Blondin, J.-M. Latour, G. Rajaraman and D. Maiti, *Chem. Sci.*, 2018, **9**, 7843–7858.
30 J. Qian, Q. An, A. Fortunelli, R. J. Nielsen and W. A. Goddard III, *J. Am. Chem. Soc.*, 2018, **140**, 6288–6297.
31 D. J. Schild, L. Nurdin, M.-E. Moret, P. H. Oyala and J. C. Peters, *Angew. Chem., Int. Ed.*, 2022, **61**, e202209655.
32 K. C. MacLeod, S. F. McWilliams, B. Q. Mercado and P. L. Holland, *Chem. Sci.*, 2016, **7**, 5736–5746.
33 Y. Ashida, T. Mizushima, K. Arashiba, A. Egi, H. Tanaka, K. Yoshizawa and Y. Nishibayashi, *Nat. Synth.*, 2023, **2**, 635–644.
34 T. Nakamura, Y. Tsuruta, A. Egi, H. Tanaka, Y. Nishibayashi and K. Yoshizawa, *Inorg. Chem.*, 2025, **64**, 9124–9136.
35 D. A. Iovan and T. A. Betley, *J. Am. Chem. Soc.*, 2016, **138**, 1983–1993.
36 K. Wu and C.-M. Che, *Chem. Commun.*, 2024, **60**, 13998–14011.
37 J. Xiong, Q. Liu, B. Lavina, M. Y. Hu, J. Zhao, E. E. Alp, L. Deng, S. Ye and Y. Guo, *Chem. Sci.*, 2023, **14**, 2808–2820.
38 S. A. Cramer and D. M. Jenkins, *J. Am. Chem. Soc.*, 2011, **133**, 19342–19345.
39 P. P. Chandrachud and D. M. Jenkins, *Encyclopedia of Inorganic and Bioinorganic Chemistry*, 2017, pp. 1–11, DOI: 10.1002/9781119951438.eibc2516.
40 C. Damiano, D. Intrieri and E. Gallo, *Inorg. Chim. Acta*, 2018, **470**, 51–67.
41 G. Coin, R. Patra, S. Rana, J. P. Biswas, P. Dubourdeaux, M. Clémancey, S. P. de Visser, D. Maiti, P. Maldivi and J.-M. Latour, *ACS Catal.*, 2020, **10**, 10010–10020.
42 C. A. Hoefer, N. K. Dietl, G. G. Zámbó, T. P. Schlachta, R. M. Reich and F. E. Kühn, *J. Organomet. Chem.*, 2024, **1006**, 123018.
43 J. A. Valdez-Moreira, D. M. Beagan, H. Yang, J. Telser, B. M. Hoffman, M. Pink, V. Carta and J. M. Smith, *ACS Cent. Sci.*, 2021, **7**, 1751–1755.
44 S. D. Brown, T. A. Betley and J. C. Peters, *J. Am. Chem. Soc.*, 2003, **125**, 322–323.
45 M. Keilwerth, W. Mao, S. A. V. Jannuzzi, L. Grunwald, F. W. Heinemann, A. Scheurer, J. Sutter, S. DeBeer, D. Munz and K. Meyer, *J. Am. Chem. Soc.*, 2023, **145**, 873–887.
46 R. E. Cowley, N. J. DeYonker, N. A. Eckert, T. R. Cundari, S. DeBeer, E. Bill, X. Ottenwaelder, C. Flaschenriem and P. L. Holland, *Inorg. Chem.*, 2010, **49**, 6172–6187.
47 A. Gonzalez, A. Casnati, M. Willingshofer, A. Radovic, G. E. Cutsail, S. Demeshko, F. Meyer and C. G. Werncke, *Chem. Commun.*, 2025, **61**, 18440–18443.
48 C. E. MacBeth, A. P. Golombek, V. G. Young, C. Yang, K. Kuczera, M. P. Hendrich and A. S. Borovik, *Science*, 2000, **289**, 938–941.
49 M. J. T. Wilding, D. A. Iovan and T. A. Betley, *J. Am. Chem. Soc.*, 2017, **139**, 12043–12049.
50 A. C. Bowman, C. Milsmann, E. Bill, Z. R. Turner, E. Lobkovsky, S. DeBeer, K. Wieghardt and P. J. Chirik, *J. Am. Chem. Soc.*, 2011, **133**, 17353–17369.
51 M. R. Anneser, G. R. Elpitiya, J. Townsend, E. J. Johnson, X. B. Powers, J. F. DeJesus, K. D. Vogiatzis and D. M. Jenkins, *Angew. Chem., Int. Ed.*, 2019, **58**, 8115–8118.
52 J.-U. Rohde, J.-H. In, M. H. Lim, W. W. Brennessel, M. R. Bukowski, A. Stubna, E. Münck, W. Nam and L. Que, *Science*, 2003, **299**, 1037–1039.
53 S. Meyer, I. Klawitter, S. Demeshko, E. Bill and F. Meyer, *Angew. Chem., Int. Ed.*, 2013, **52**, 901–905.
54 C. M. Thomas, N. P. Mankad and J. C. Peters, *J. Am. Chem. Soc.*, 2006, **128**, 4956–4957.
55 J. England, Y. Guo, E. R. Farquhar, V. G. Young Jr, E. Münck and L. Que Jr, *J. Am. Chem. Soc.*, 2010, **132**, 8635–8644.
56 K. Warm, A. Paskin, U. Kuhlmann, E. Bill, M. Swart, M. Haumann, H. Dau, P. Hildebrandt and K. Ray, *Angew. Chem., Int. Ed.*, 2021, **60**, 6752–6756.
57 I. Nieto, F. Ding, R. P. Bontchev, H. Wang and J. M. Smith, *J. Am. Chem. Soc.*, 2008, **130**, 2716–2717.
58 W. Mao, Z. Zhang, M. Keilwerth, H. Chen, F. W. Heinemann, A. Scheurer, S. DeBeer, F. Neese and K. J. Meyer, *Am. Chem. Soc.*, 2026, Just Accepted.
59 K. D. Vogiatzis, M. V. Polynski, J. K. Kirkland, J. Townsend, A. Hashemi, C. Liu and E. A. Pidko, *Chem. Rev.*, 2019, **119**, 2453–2523.
60 W. M. C. Sameera and F. Maseras, *Wiley Interdiscip. Rev.: Comput. Mol. Sci.*, 2012, **2**, 375–385.
61 A. J. Cohen, P. Mori-Sánchez and W. Yang, *J. Chem. Phys.*, 2008, **129**, 204112.
62 P. Verma and D. G. Truhlar, *Trends Chem.*, 2020, **2**, 302–318.
63 S. Per, H. Anders, R. Björn and L. Bernard, *Phys. Scr.*, 1980, **21**, 323.
64 K. Andersson, P. A. Malmqvist, B. O. Roos, A. J. Sadlej and K. Wolinski, *J. Phys. Chem.*, 1990, **94**, 5483–5488.
65 C. Angeli, R. Cimiraglia, S. Evangelisti, T. Leininger and J.-P. Malrieu, *J. Chem. Phys.*, 2001, **114**, 10252–10264.
66 K. D. Vogiatzis, D. Ma, J. Olsen, L. Gagliardi and W. A. de Jong, *J. Chem. Phys.*, 2017, **147**, 184111.
67 G. Li Manni, S. D. Smart and A. Alavi, *J. Chem. Theory Comput.*, 2016, **12**, 1245–1258.
68 S. R. White, *Phys. Rev. Lett.*, 1992, **69**, 2863–2866.
69 K. H. Marti and M. Reiher, *Z. Physiol. Chem.*, 2010, **224**, 583–599.
70 A. Baiardi and M. Reiher, *J. Chem. Phys.*, 2020, **152**, 040903.
71 G. Li Manni, D. Kats, D. P. Tew and A. Alavi, *J. Chem. Theory Comput.*, 2019, **15**, 1492–1497.

72 R. Olivares-Amaya, W. Hu, N. Nakatani, S. Sharma, J. Yang and G. K.-L. Chan, *J. Chem. Phys.*, 2015, **142**, 034102.
73 C. Riplinger and F. Neese, *J. Chem. Phys.*, 2013, **138**, 034106.
74 M. Drosou, C. A. Mitsopoulou and D. A. Pantazis, *J. Chem. Theory Comput.*, 2022, **18**, 3538–3548.
75 R. Kumar, A. Ansari, P. Comba and G. Rajaraman, *Chem. – Eur. J.*, 2024, **30**, e202303300.
76 M. Kumar, M. K. Gupta, M. Ansari and A. Ansari, *Phys. Chem. Chem. Phys.*, 2024, **26**, 4349–4362.
77 A. Pyykkönen, A. Wodyński, M. Kaupp and J. Vaara, *Phys. Chem. Chem. Phys.*, 2025, **27**, 18887–18900.
78 A. Warshel and M. Levitt, *J. Mol. Biol.*, 1976, **103**, 227–249.
79 C. E. Tzeliou, M. A. Mermigki and D. Tzeli, *Molecules*, 2022, **27**, 2660.
80 J. Xia, Y. Zhang and B. Jiang, *Chem. Soc. Rev.*, 2025, **54**, 4790–4821.
81 K. D. Vogiatzis, C. Corminboeuf, A. Nova, K. Jorner, J. Kästner, M. Meuwly, P. Schwaller, V. Böttcher, M. Drosou, E. Fako, H. Hoppe, Z. Ivkovic, N. Iwanojko, D. A. Pantazis, S. P. Schmid, K. Szenes, A. Tetenoire and M. Reiher, *J. Am. Chem. Soc.*, 2026, **148**, 9143–9155, DOI: 10.1021/jacs.5c17786.
82 K. Ray, F. Heims and F. F. Pfaff, *Eur. J. Inorg. Chem.*, 2013, **2013**, 3784–3807.
83 A. Bhardwaj and B. Mondal, *Inorg. Chem.*, 2024, **63**, 14468–14481.
84 E. Tangen, J. Conradie and A. Ghosh, *J. Chem. Theory Comput.*, 2007, **3**, 448–457.
85 H. Chen, W. Lai and S. Shaik, *J. Phys. Chem. Lett.*, 2010, **1**, 1533–1540.
86 J. Conradie, E. Tangen and A. Ghosh, *J. Inorg. Biochem.*, 2006, **100**, 707–715.
87 V. A. Larson, B. Battistella, K. Ray, N. Lehnert and W. Nam, *Nat. Rev. Chem.*, 2020, **4**, 404–419.
88 G. Sabenya, I. Gamba, L. Gómez, M. Clémancey, J. R. Frisch, E. J. Klinker, G. Blondin, S. Torelli, L. Que, V. Martin-Diaconescu, J.-M. Latour, J. Lloret-Fillol and M. Costas, *Chem. Sci.*, 2019, **10**, 9513–9529.
89 C. T. Saouma and J. C. Peters, *Coord. Chem. Rev.*, 2011, **255**, 920–937.
90 C. Kupper, B. Mondal, J. Serrano-Plana, I. Klawitter, F. Neese, M. Costas, S. Ye and F. Meyer, *J. Am. Chem. Soc.*, 2017, **139**, 8939–8949.
91 J. F. Berry, S. DeBeer George and F. Neese, *Phys. Chem. Chem. Phys.*, 2008, **10**, 4361–4374.
92 T. Birk and J. Bendix, *Inorg. Chem.*, 2003, **42**, 7608–7615.
93 Q. Liu, L. Long, P. Ma, Y. Ma, X. Leng, J. Xiao, H. Chen and L. Deng, *Cell Rep. Phys. Sci.*, 2021, **2**, 100454.
94 J. J. Scepaniak, M. D. Fulton, R. P. Bontchev, E. N. Duesler, M. L. Kirk and J. M. Smith, *J. Am. Chem. Soc.*, 2008, **130**, 10515–10517.
95 J. G. Gardner, J. E. Schneider and J. S. Anderson, *Inorg. Chem.*, 2021, **60**, 13854–13860.
96 S. D. Brown and J. C. Peters, *J. Am. Chem. Soc.*, 2005, **127**, 1913–1923.
97 S. Ye and F. Neese, *Proc. Natl. Acad. Sci. U. S. A.*, 2011, **108**, 1228–1233.
98 S. Ye and F. Neese, *Curr. Opin. Chem. Biol.*, 2009, **13**, 89–98.
99 B. K. Mai and Y. Kim, *Inorg. Chem.*, 2016, **55**, 3844–3852.
100 C. Geng, S. Ye and F. Neese, *Angew. Chem., Int. Ed.*, 2010, **49**, 5717–5720.
101 J. K. Kirkland, S. N. Khan, B. Casale, E. Miliordos and K. D. Vogiatzis, *Phys. Chem. Chem. Phys.*, 2018, **20**, 28786–28795.
102 S. Sahu, L. R. Widger, M. G. Quesne, S. P. de Visser, H. Matsumura, P. Moënne-Loccoz, M. A. Siegler and D. P. Goldberg, *J. Am. Chem. Soc.*, 2013, **135**, 10590–10593.
103 A. Braun, L. B. Gee, M. W. Mara, E. A. Hill, T. Kroll, D. Nordlund, D. Sokaras, P. Glatzel, B. Hedman, K. O. Hodgson, A. S. Borovik, M. L. Baker and E. I. Solomon, *J. Am. Chem. Soc.*, 2023, **145**, 18977–18991.
104 A. Decker, J.-U. Rohde, E. J. Klinker, S. D. Wong, L. Que and E. I. Solomon, *J. Am. Chem. Soc.*, 2007, **129**, 15983–15996.
105 P. C. Andrikopoulos, C. Michel, S. Chouzier and P. Sautet, *ACS Catal.*, 2015, **5**, 2490–2499.
106 P. Comba, G. Nunn, F. Scherz and P. H. Walton, *Faraday Discuss.*, 2022, **234**, 232–244.
107 C. V. Sastri, J. Lee, K. Oh, Y. J. Lee, J. Lee, T. A. Jackson, K. Ray, H. Hirao, W. Shin, J. A. Halfen, J. Kim, L. Que, S. Shaik and W. Nam, *Proc. Natl. Acad. Sci. U. S. A.*, 2007, **104**, 19181–19186.
108 J.-U. Rohde and L. Que Jr, *Angew. Chem., Int. Ed.*, 2005, **44**, 2255–2258.
109 A. Kazaryan and E. J. Baerends, *ACS Catal.*, 2015, **5**, 1475–1488.
110 L. Bernasconi, M. J. Louwerse and E. J. Baerends, *Eur. J. Inorg. Chem.*, 2007, **2007**, 3023–3033.
111 W. Rasheed, A. Draksharapu, S. Banerjee, V. G. Young Jr, R. Fan, Y. Guo, M. Ozerov, J. Nehrkorn, J. Krzystek, J. Telser and L. Que Jr, *Angew. Chem., Int. Ed.*, 2018, **57**, 9387–9391.
112 G. Mukherjee, C. W. Z. Lee, S. S. Nag, A. Alili, F. G. Cantú Reinhard, D. Kumar, C. V. Sastri and S. P. de Visser, *Dalton Trans.*, 2018, **47**, 14945–14957.
113 J. England, J. Prakash, M. A. Cranswick, D. Mandal, Y. Guo, E. Münck, S. Shaik and L. Que Jr, *Inorg. Chem.*, 2015, **54**, 7828–7839.
114 A. Sen, S. Sharma and G. Rajaraman, *Angew. Chem., Int. Ed.*, 2025, **64**, e202419953.
115 M. J. T. Wilding, D. A. Iovan, A. T. Wrobel, J. T. Lukens, S. N. MacMillan, K. M. Lancaster and T. A. Betley, *J. Am. Chem. Soc.*, 2017, **139**, 14757–14766.
116 M. Mahajan and B. Mondal, *Inorg. Chem.*, 2023, **62**, 5810–5821.
117 B. Pandey, M. Jaccob and G. Rajaraman, *Chem. Commun.*, 2017, **53**, 3193–3196.

118 S. Kumar, A. S. Faponle, P. Barman, A. K. Vardhaman, C. V. Sastri, D. Kumar and S. P. de Visser, *J. Am. Chem. Soc.*, 2014, **136**, 17102–17115.
119 T. Josephy, R. Kumar, K. Bleher, F. Röhs, T. Glaser, G. Rajaraman and P. Comba, *Inorg. Chem.*, 2024, **63**, 12109–12119.
120 E. Andris, K. Segers, J. Mehara, L. Rulíšek and J. Roithová, *Angew. Chem., Int. Ed.*, 2020, **59**, 23137–23144.
121 Y. Cao, J. A. Valdez-Moreira, S. Hay, J. M. Smith and S. P. de Visser, *Chem. – Eur. J.*, 2023, **29**, e202300271.
122 D. Schröder, S. Shaik and H. Schwarz, *Acc. Chem. Res.*, 2000, **33**, 139–145.
123 A. Ansari, A. Kaushik and G. Rajaraman, *J. Am. Chem. Soc.*, 2013, **135**, 4235–4249.
124 Monika and A. Ansari, *New J. Chem.*, 2020, **44**, 19103–19112.
125 P. Barman, A. K. Vardhaman, B. Martin, S. J. Wörner, C. V. Sastri and P. Comba, *Angew. Chem., Int. Ed.*, 2015, **54**, 2095–2099.
126 S. Hong, K. D. Sutherlin, A. K. Vardhaman, J. J. Yan, S. Park, Y.-M. Lee, S. Jang, X. Lu, T. Ohta, T. Ogura, E. I. Solomon and W. Nam, *J. Am. Chem. Soc.*, 2017, **139**, 8800–8803.
127 J. K. Satpathy, R. Yadav, L. Sahoo, J. Uhlig, E. Nordlander, C. V. Sastri and S. P. de Visser, *Chem. Sci.*, 2026, **17**, 1349–1364.
128 A. Bhardwaj and B. Mondal, *Inorg. Chem.*, 2025, **64**, 14999–15010.
129 E. Andris, R. Navrátil, J. Jašík, M. Srnec, M. Rodríguez, M. Costas and J. Roithová, *Angew. Chem., Int. Ed.*, 2019, **58**, 9619–9624.
130 S. Ye, C. Kupper, S. Meyer, E. Andris, R. Navrátil, O. Krahe, B. Mondal, M. Atanasov, E. Bill, J. Roithová, F. Meyer and F. Neese, *J. Am. Chem. Soc.*, 2016, **138**, 14312–14325.
131 M. L. Neidig, A. Decker, O. W. Choroba, F. Huang, M. Kavana, G. R. Moran, J. B. Spencer and E. I. Solomon, *Proc. Natl. Acad. Sci. U. S. A.*, 2006, **103**, 12966–12973.
132 A. Braun, L. B. Gee, M. D. J. Waters, M. L. Baker, M. W. Mara, A. Zhou, T. Kroll, D. Nordlund, D. Sokaras, B. Hedman, K. O. Hodgson, L. Que Jr and E. I. Solomon, *J. Am. Chem. Soc.*, 2024, **146**, 35139–35145.
133 M. Srnec, S. D. Wong, J. England, L. Que and E. I. Solomon, *Proc. Natl. Acad. Sci. U. S. A.*, 2012, **109**, 14326–14331.
134 M. Srnec, S. R. Iyer, L. M. K. Dassama, K. Park, S. D. Wong, K. D. Sutherlin, Y. Yoda, Y. Kobayashi, M. Kurokuzu, M. Saito, M. Seto, C. Krebs, J. M. Bollinger Jr and E. I. Solomon, *J. Am. Chem. Soc.*, 2020, **142**, 18886–18896.
135 M. Srnec, S. D. Wong, M. L. Matthews, C. Krebs, J. M. Bollinger Jr and E. I. Solomon, *J. Am. Chem. Soc.*, 2016, **138**, 5110–5122.
136 S. Pattanayak, F. G. Cantú Reinhard, A. Rana, S. S. Gupta and S. P. de Visser, *Chem. – Eur. J.*, 2019, **25**, 8092–8104.
137 B. A. Smith, S. Hakimov, D. M. Jenkins and K. D. Vogiatzis, *Dalton Trans.*, 2024, **53**, 14665–14677.
138 M. Srnec and E. I. Solomon, *J. Am. Chem. Soc.*, 2017, **139**, 2396–2407.
139 M. G. Thomas, S. B. J. S. Rifayee, S. S. Chaturvedi, K. R. Gorantla, W. White, J. Wildey, C. J. Schofield and C. Z. Christov, *Inorg. Chem.*, 2024, **63**, 10737–10755.
140 S. O. Waheed, S. S. Chaturvedi, T. G. Karabencheva-Christova and C. Z. Christov, *ACS Catal.*, 2021, **11**, 3877–3890.
141 S. S. Chaturvedi, S. B. J. S. Rifayee, S. O. Waheed, J. Wildey, C. Warner, C. J. Schofield, T. G. Karabencheva-Christova and C. Z. Christov, *JACS Au*, 2022, **2**, 2169–2186.
142 E. S. Wenger, R. J. Martinie, R. Ushimaru, C. J. Pollock, D. Sil, A. Li, N. Hoang, G. M. Palowitch, B. P. Graham, I. Schaperdoth, E. J. Burke, A. O. Maggiolo, W.-c. Chang, B. D. Allen, C. Krebs, A. Silakov, A. K. Boal and J. M. Bollinger Jr, *J. Am. Chem. Soc.*, 2024, **146**, 24271–24287.
143 S. D. Wong, M. Srnec, M. L. Matthews, L. V. Liu, Y. Kwak, K. Park, C. B. Bell III, E. E. Alp, J. Zhao, Y. Yoda, S. Kitao, M. Seto, C. Krebs, J. M. Bollinger and E. I. Solomon, *Nature*, 2013, **499**, 320–323.
144 Y.-C. Zheng, X. Li, L. Cha, J. C. Paris, C. Michael, R. Ushimaru, Y. Ogasawara, I. Abe, Y. Guo and W.-c. Chang, *J. Am. Chem. Soc.*, 2025, **147**, 6162–6170.
145 R. Ushimaru, R. Chen, P.-H. Fan, X. Liu, M. W. Ruszczycky and H.-w. Liu, *J. Am. Chem. Soc.*, 2025, **147**, 46543–46549.
146 A. K. Vardhaman, P. Barman, S. Kumar, C. V. Sastri, D. Kumar and S. P. de Visser, *Angew. Chem., Int. Ed.*, 2013, **52**, 12288–12292.
147 M. L. Matthews, C. S. Neumann, L. A. Miles, T. L. Grove, S. J. Booker, C. Krebs, C. T. Walsh and J. M. Bollinger, *Proc. Natl. Acad. Sci. U. S. A.*, 2009, **106**, 17723–17728.
148 D. W. Kastner, A. Nandy, R. Mehmood and H. J. Kulik, *ACS Catal.*, 2023, **13**, 2489–2501.
149 F. Ahsan, M. Ansari, J. E. M. N. Klein and M. Swart, *J. Inorg. Biochem.*, 2025, **272**, 112989.
150 A. Kluza, Z. Wojdyla, B. Mrugala, K. Kurpiewska, P. J. Porebski, E. Niedzialkowska, W. Minor, M. S. Weiss and T. Borowski, *Dalton Trans.*, 2020, **49**, 4454–4469.
151 S. Sahu, M. G. Quesne, C. G. Davies, M. Dürr, I. Ivanović-Burmazović, M. A. Siegler, G. N. L. Jameson, S. P. de Visser and D. P. Goldberg, *J. Am. Chem. Soc.*, 2014, **136**, 13542–13545.
152 M. P. Jensen, M. P. Mehn and L. Que Jr, *Angew. Chem., Int. Ed.*, 2003, **42**, 4357–4360.
153 A. Nandy, J. Zhu, J. P. Janet, C. Duan, R. B. Getman and H. J. Kulik, *ACS Catal.*, 2019, **9**, 8243–8255.
154 G. M. Jones, B. A. Smith, J. K. Kirkland and K. D. Vogiatzis, *Inorg. Chem. Front.*, 2023, **10**, 1062–1075.
155 A. Nandy, C. Duan, C. Goffinet and H. J. Kulik, *JACS Au*, 2022, **2**, 1200–1213.

